J. Fluid Mech. (2023), *vol*. 970, A13, doi:10.1017/jfm.2023.614

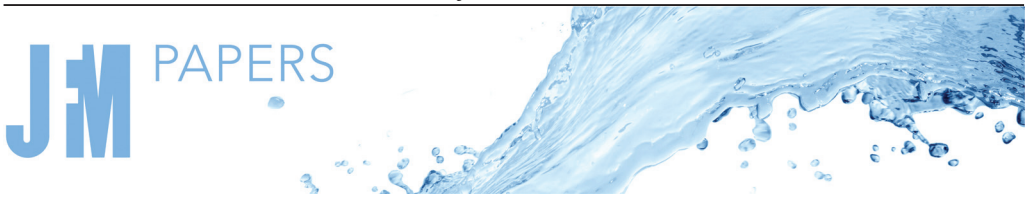

Effects of surfactants on bubble-induced turbulence

Tian Ma[1],†, **Hendrik Hessenkemper**[1],†, **Dirk Lucas**[1] **and Andrew D. Bragg**[2],†

[1]Helmholtz-Zentrum Dresden – Rossendorf, Institute of Fluid Dynamics, 01328 Dresden, Germany

[2]Department of Civil and Environmental Engineering, Duke University, Durham, NC 27708, USA

(Received 6 December 2022; revised 19 July 2023; accepted 20 July 2023)

We use experiments to explore the effect of surfactants on bubble-induced turbulence (BIT) at different scales, considering how the bubbles affect the flow kinetic energy, anisotropy and extreme events. To this end, high-resolution particle shadow velocimetry measurements are carried out in a bubble column in which the flow is generated by bubble swarms rising in water for two different bubble diameters (3 and 4 mm) and moderate gas volume fractions (0.5 %–1.3 %). We use tap water as the base liquid and add 1-Pentanol as an additional surfactant with varying bulk concentration, leading to different bubble shapes and surface boundary conditions. The results reveal that with increasing surfactant concentration, the BIT generated increases in strength, even though bubbles of a given size rise more slowly with surfactants. We also find that the level of anisotropy in the flow is enhanced with increasing surfactant concentration for bubbles of the same size, and that for the same surfactant concentration, smaller bubbles generate stronger anisotropy in the flow. Concerning the intermittency quantified by the normalized probability density functions of the fluid velocity increments, our results indicate that extreme values in the velocity increments become more probable with decreasing surfactant concentration for cases with smaller bubbles and low gas void fraction, while the effect of the surfactant is much weaker for cases with larger bubble and higher void fractions.

Key words: drops and bubbles, multiphase and particle-laden flows, turbulent flows

1. Introduction

Surfactants are ‘surface-active’ molecules and/or particles that are easily adsorbed at surfaces and form monolayers (Langevin 2014; Manikantan & Squires 2020). They are

† Email addresses for correspondence: tian.ma@hzdr.de, h.hessenkemper@hzdr.de, andrew.bragg@duke.edu

present in most multiphase systems, being either present naturally or else introduced purposefully (Levich 1962; Stone 1994; Soligo, Roccon & Soldati 2019; Lohse 2022). In bubbly flows, it has been shown that even small amounts of surfactant can cause dramatic changes to the bubble shapes (Tomiyama *et al.* 2002; Tagawa, Takagi & Matsumoto 2014; Hessenkemper *et al.* 2021*a*), bubble rise velocities (Bel Fdhila & Duineveld 1996; Cuenot, Magnaudet & Spennato 1997; Takagi, Ogasawara & Matsumoto 2008; Tagawa *et al.* 2014), lateral migration (Lu, Muradoglu & Tryggvason 2017; Hayashi & Tomiyama 2018; Ahmed *et al.* 2020; Atasi *et al.* 2023), cluster formation (Takagi *et al.* 2009; Maeda *et al.* 2021; Ma *et al.* 2023), coalescence (Verschoof *et al.* 2016; Lohse 2018; Néel & Deike 2021) and mass transfer on the interfaces (Cuenot *et al.* 1997; Schlüter *et al.* 2021). Some of the aforementioned effects can also occur due to the presence of salt in the liquid phase (Craig, Ninham & Pashley 1993; Gvozdić *et al.* 2019; Hori *et al.* 2020; Blaauw, Lohse & Huisman 2023), However, the mechanisms producing these effects are different in that case.

The mechanism by which surfactants influence the velocity field in the vicinity of a gas–liquid interface was first introduced by Frumkin & Levich (1947) and Levich (1962), who showed that as a bubble rises in an aqueous surfactant solution, surfactant is swept off the front part of the bubble by surface convection, and accumulates in the rear region. They lower the surface tension in the rear region relative to that at the front, leading to a gradient of surface tension along the interface. This gradient creates a tangential shear stress on the bubble surface (Marangoni effect) that opposes the surface flow, causes the interface to become more rigid, and increases the drag coefficient C_D. The free-slip boundary condition that occurs at a gas–liquid interface for an ideal purified system (e.g. 'hyper-clean' water) breaks down, and the rise speed of the contaminated bubble decreases with increasing surfactant concentration, approaching the behaviour of a rigid body for sufficient surfactant concentration.

The effect of drag coefficient increase due to the adsorption of surfactants has been studied in great detail. Readers are referred to Magnaudet & Eames (2000), Palaparthi, Papageorgiou & Maldarelli (2006) and Takagi & Matsumoto (2011) for detailed reviews from the perspective of hydrodynamics, and Manikantan & Squires (2020) from the perspective of surfactant dynamics. An early study (Bachhuber & Sanford 1974) measured the terminal velocity of small bubbles (bubble Reynolds number $Re_p \sim O(10)$) rising in distilled water at two heights in the flow, and observed that the velocity at the lower height was in good agreement with that expected for a clean spherical bubble, while that measured at the greater height was consistent with a particle having a value of C_D that corresponds to a rigid sphere. Their interesting observation reflects at least two well-known aspects of how surfactants impact bubble motion. First, water used in typical lab conditions is contaminated, possibly containing considerable amounts of surfactants that can influence the motion of bubbles. Second, it takes a finite time (which depends on the properties of the surfactants) for the surfactants to be adsorbed at the bubble surface before reaching an equilibrium state, with the implication that bubble rise velocities decrease with increasing travel distance until reaching a constant value (Durst *et al.* 1986; Tagawa *et al.* 2014; Hessenkemper *et al.* 2021*a*).

The fact that the bubble rise velocity decreases in the presence of surfactants also leads to a smaller inertial force experienced by bubbles. As a result of this, for a fixed bubble size, the bubble shape is less flattened in a contaminated system than it is in a purified system, despite the fact that surface tension is reduced by surfactants.

The aforementioned modifications in bubble rise velocity, surface boundary condition and shape due to surfactants have a strong impact on the wake structure and the path instability of a rising bubble. Tagawa *et al.* (2014) used experiments to investigate the

effect of surfactants on the path instability of an air bubble rising in quiescent water, and categorized the rising bubble trajectories as straight, helical or zigzag based on the bubble Reynolds number and surface slip condition. They observed that the trajectory of the bubble was first helical and then transitioned to a zigzag motion in Triton X-100 solution – a phenomenon never reported in purified water (Mougin & Magnaudet 2002; Shew & Pinton 2006). Pesci *et al.* (2018) used numerical simulations to study the effects of soluble surfactants on the dynamics of a single spheroidal bubble rising in a large spherical domain. They found that if the surface contamination is sufficiently high, then a quasi-steady bubble velocity can be obtained over a wide range of surfactant concentrations, independent of the exact concentration value in the bulk. Furthermore, they also observed a transition from a helical to a zigzag rising bubble trajectory, as reported experimentally by Tagawa *et al.* (2014), but also found that the nature of the trajectory depends on both the initial surface and bulk surfactant contamination. Pesci *et al.* (2018) also looked at the vorticity dynamics in the vicinity of the bubble, and observed strong vorticity production very close to the bubble surface due to Marangoni forces, while in clean water this production is much weaker (see the vorticity distribution in figure 8 of Mougin & Magnaudet 2006). Legendre, Lauga & Magnaudet (2009) performed numerical simulations to study the two-dimensional flow past a cylinder, and investigated the influence of a generic slip boundary condition on the wake dynamics. They showed that slip markedly decreases the vorticity intensity in the wake. Mclaughlin (1996) and Cuenot *et al.* (1997) used a stagnant-cap approximation to compare the wake structure produced by contaminated bubbles and solid spheres. The former study revealed that the wake volume for contaminated bubbles is larger than for solid spheres moving at the same Reynolds number, and the latter study found that the wake length is larger for contaminated bubbles. They explained that the increase of the wake size is caused by the abrupt change to the dynamic boundary condition where the transition from a quasi-shear-free (the upper part of the bubble) to a quasi-no-slip (the rear region) condition generates strong vorticity at the interface. As a result, there is more vorticity injected into the flow for contaminated bubbles than for a rigid sphere with a uniform no-slip condition, resulting in a larger wake.

The observations summarized above were mainly for isolated bubbles in the absence of turbulence. Swarms of bubbles can, however, induce strong background turbulence, and the observations above could indicate that turbulence generated by wakes in bubble swarms could depend strongly on the degree of contamination in the fluid. Direct numerical simulations (DNS) have revealed the following properties of dilute dispersed bubbly flows. (i) The liquid velocity fluctuations are highly anisotropic, with fluctuations that are much larger in the direction of the mean bubble motion (Lu & Tryggvason 2013; Ma *et al.* 2020*b*; Ma, Lucas & Bragg 2020*a*; du Cluzeau *et al.* 2022; Liao & Ma 2022). It was demonstrated recently that this strong anisotropy also exists at the small scales of bubble-induced turbulence (BIT) due to the energy being injected at the scale of the bubble (Ma *et al.* 2021). (ii) The probability density functions (PDFs) of all fluctuating velocity components are non-Gaussian, with the PDF of the vertical velocity fluctuations being strongly positively skewed, while the other two directions have symmetric PDFs (Roghair *et al.* 2011; Riboux, Legendre & Risso 2013). (iii) There is strong enhancement of the turbulent kinetic energy dissipation rate in the vicinity of the bubble surface (Santarelli, Roussel & Fröhlich 2016; du Cluzeau, Bois & Toutant 2019). (iv) The energy spectra in either the frequency or wavenumber space exhibit a -3 power-law scaling for a subrange for all the components of the fluctuating fluid velocity (Ma *et al.* 2017; Pandey, Ramadugu & Perlekar 2020; Innocenti *et al.* 2021). (v) Pandey *et al.* (2020) and Innocenti *et al.* (2021) showed that on average, the energy transfer is from large to small scales in BIT;

however, there is also evidence of an upscale transfer when considering the transfer of energy associated with particular components of the velocity field (Ma *et al.* 2021). (vi) For a bubbly flow with background turbulence, the flow intermittency is increased significantly by the addition of bubbles to the flow when compared to the corresponding unladen turbulent flow with similar bulk Reynolds number (Biferale *et al.* 2012; Ma *et al.* 2021). Note that some of these DNS studies effectively considered contaminated bubbly flows since they used no-slip conditions on rigid bubble surfaces, while others used slip boundary conditions, and a clear understanding of exactly how the aforementioned properties of BIT depend on contaminants in the flow is not available. For further details on the relevant DNS studies, readers are referred to the recent reviews of Risso (2018) and Mathai, Lohse & Sun (2020).

Several experiments have also observed these properties for bubbly turbulent flows (Lance & Bataille 1991; Rensen, Luther & Lohse 2005; Riboux, Risso & Legendre 2010; Mendez-Diaz *et al.* 2013; Lai & Socolofsky 2019; Salibindla *et al.* 2020; Masuk, Salibindla & Ni 2021; Qi *et al.* 2022). However, in most of these experiments there will be some contamination in the liquid, and the impact of this on the results is not understood. Indeed, a systematic investigation into how contamination affects the properties of BIT is still missing, to the best of the authors' knowledge. Therefore, in the present paper we explore systematically the effect of surfactants on the properties of BIT produced by bubble swarms, considering both single-point and two-point turbulence statistics to characterize large- and small-scale flow properties. The rest of this paper is organized as follows. In § 2, we describe the experimental set-up and the measurement techniques. We then give a brief overview regarding the effect of the surfactant on the single-bubble behaviour in the chosen solution (§ 3), followed by a presentation of the single-point statistics for the bubble swarm in § 4. Finally, the multipoint results from the experiments that give insights into the properties of the flow at different scales are divided into two parts, namely, the flow anisotropy in § 5.1, and the extreme events in § 5.2.

2. Experimental method

2.1. *Experimental facility*

The experimental apparatus is identical to that in Ma *et al.* (2022), and we therefore refer the reader to that paper for additional details; here, we summarize. Figure 1 shows a sketch of the experimental set-up, consisting of a rectangular column (depth 50 mm and width 112.5 mm) made of acrylic glass with water fill height 1100 mm. Air bubbles are injected through 11 spargers that are distributed homogeneously at the bottom of the column.

We use tap water in the present work as the base liquid, and add 1-Pentanol as an additional surfactant with varying bulk concentration C_∞ of 0, 333 and 1000 ppm. The surfactant properties and the single-bubble behaviour in these solutions will be discussed in detail in § 3.2. Note that the tap water will already be sightly contaminated prior to adding the surfactants, and the bubbles can behave differently in this tap water without surfactants compared to that in a pure water system (no surfactants; see e.g. Veldhuis, Biesheuvel & Van Wijngaarden 2008; Takagi & Matsumoto 2011). For the bubble sizes considered in the present study (with $d_p > 2$ mm), however, the slight contamination in the tap water does not have a significant effect on the bubble motion (Ellingsen & Risso 2001). This point was also confirmed by our previous study (Hessenkemper *et al.* 2021*b*) for the bubble sizes considered here, with both the bubble rise velocity and bubble aspect ratio showing little difference between tap water and purified water systems.

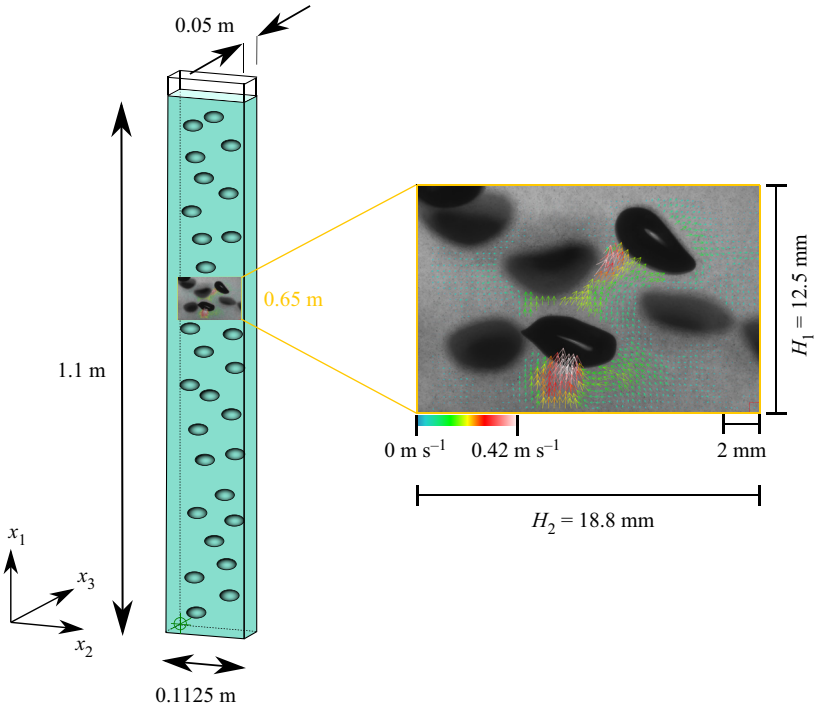

Figure 1. Sketch of the bubble column used in the experiments. (Note that in the actual experiment, the number of bubbles in the column is $O(10^3)$.) The sketch is not to scale; the column depth is many times larger than the bubble diameter. The inset shows an instantaneous realization of velocity vectors over the field of view in the case *LaTap* (see table 1), with two in-focus bubbles recognizable by their sharp interfaces and associated wakes.

We consider two different bubble sizes by using spargers with different inner diameters. For each bubble size, we maintain the same gas inlet velocity and ensure that all cases are not in the heterogeneous regime of dispersed bubbly flows. In total, we have six monodispersed cases labelled *SmTap*, *SmPen*, *SmPen+*, *LaTap*, *LaPen* and *LaPen+* in table 1, including some basic characteristic dimensionless numbers for the bubbles. We note that the Weber number based on the liquid mean fluctuating velocity is almost two orders of magnitude smaller than the Eötvös number, indicating that the bubble deformability in the present six cases is due mainly to buoyancy rather than turbulence. Further evidence for this is provided by noting that the bubble shapes are similar to those for the single-bubble cases in § 3.2, for which the liquid turbulence is much weaker. Here, *Sm*/*La* stand for smaller/larger bubbles, and *Tap*/*Pen*/*Pen+* stand for corresponding cases having 1-Pentanol concentration with $C_\infty = 0$, 333 and 1000 ppm, respectively. It should be noted that the three cases with larger bubble sizes have higher gas void fraction than the three cases with smaller bubbles. This is because in our set-up it is not possible to have the same flow rate for two different spargers while also maintaining a homogeneous gas distribution for monodispersed bubbles.

2.2. *Flow imaging*

2.2.1. *Liquid phase*

For all measurements stated below, we use a 2.5 megapixel CMOS camera (Imaging Solutions) equipped with a 100 mm focal length macro lens (Samyang). To measure the

Parameter	*SmTap*	*SmPen*	*SmPen+*	*LaTap*	*LaPen*	*LaPen+*
C_∞ (ppm)	0	333	1000	0	333	1000
α	0.46 %	0.47 %	0.54 %	1.36 %	1.33 %	1.33 %
d_p (mm)	3	2.5	2.6	4.1	3.8	3.8
χ	1.8	1.3	1.2	1.8	1.5	1.3
σ (N m^{-1})	0.072	0.070	0.067	0.072	0.070	0.067
Ga	504	394	420	815	729	719
Eo	1.27	0.91	0.99	2.4	2.07	2.03
We	0.011	0.010	0.017	0.053	0.050	0.062
U_r (m s^{-1})	0.27	0.23	0.20	0.24	0.23	0.22
Re_p	798	587	528	986	866	817
C_D	0.53	0.60	0.84	0.90	0.93	1.02

Table 1. Selected characteristics of the six bubble swarm cases investigated. Here, C_∞ is the bulk concentration of 1-Pentanol, α is the averaged gas void fraction, d_p is the equivalent bubble diameter, χ is the aspect ratio, $Ga \equiv \sqrt{|\pi_\rho - 1|\, g d_p^3/\nu}$ is the Galileo number, $Eo \equiv \Delta\rho\, g d_p^2/\sigma$ is the Eötvös number, $We \equiv \rho d_p u^{*2}/\sigma$ is the Weber number, and u^* is the mean fluctuating velocity. The values of Re_p, the bubble Reynolds number, and C_D, the drag coefficient, are based on d_p and the slip velocity U_r obtained from the experiment.

liquid velocity, we use particle shadow velocimetry (PSV), which is similar to planar particle image velocimetry (PIV) with the only difference being that backlight illumination together with a shallow depth of field (DoF) is used. The velocity is then determined by correlating the displacement of sharp tracer particles inside a narrow sharpness region. A detailed description of the image processing procedure used can be found in Hessenkemper & Ziegenhein (2018). The measurement set-up and data acquisition are similar to those in our previous work (Ma *et al.* 2022), so only the key aspects for the liquid velocity measurements are stated in what follows.

The liquid velocity measurements take place along the x_1–x_2 symmetry plane in the centre of the depth (x_3). The measurement height with $x_1 = 0.65$ m is based on the centre of the field of view (FOV) (figure 1). We use 10 µm hollow glass spheres (Dantec) as tracer particles, with estimated Stokes number $O(10^{-3})$; they are hydrophilic and so are not adsorbed by the bubble surface. The flow section is illuminated with a 200 W LED lamp and f-stop 2.8 is set at the camera lens to provide an effective shallow DoF ∼370 µm. The captured images cover a FOV 18.8 mm (H_2) × 12.5 mm (H_1), which results in pixel size 9.8 µm. For each case, 15 000 image pairs are recorded, with a time delay of approximately 0.5 s before the next image pair is acquired, providing 15 000 uncorrelated velocity fields. The comparatively large bubble shadows in the images are masked, and the corresponding areas are not considered in the following correlation step. The final interrogation window is 64 × 64 pixels with 50 % overlap, resulting in vector spacing 0.627 mm. Here, we use standard PIV processing steps to determine the velocity, including multipass/window refinement steps and universal outlier detection. A representative transient FOV for the case *LaTap* is shown in figure 1, overlaid with the resulting liquid velocity vector field. In this figure, two in-focus bubbles can be identified by their sharp interfaces and the associated wakes in the velocity vector field.

2.2.2. *Gas phase*

Similar to our previous work (Ma *et al.* 2022), compared to the liquid phase we use a larger FOV (40 mm × 80 mm) for the gas phase to capture the bubble statistics in all the

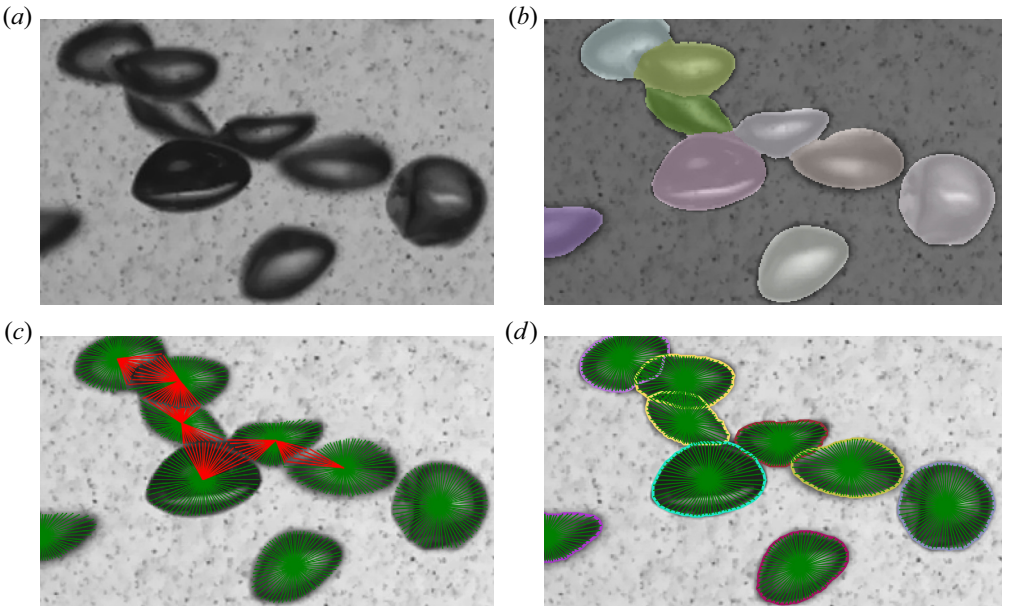

Figure 2. (*a*) Example image of the bubbles from a fragment in the middle of figure 3(*b*), identified by the area marked with white dashed line there for the *LaTap* case. (*b–d*) Three steps to reconstruct hidden bubble parts for an irregular shaped bubble: (*b*) segmentation mask, (*c*) radial distances, and (*d*) corrected radial distances.

cases considered. For sufficient statistics, 1500 image pairs are evaluated at frame rate 500 f.p.s. The bubbles are detected with a novel convolutional neural network (CNN) based bubble identification algorithm, which is trained to segment bubbles in crowded situations (coloured patches in figure 2*b*). Furthermore, the hidden part of a partly occluded bubble is estimated with an additionally trained neural network. For this, equal numbers of radial rays are generated for the identified segments, starting from the segment centre to its boundary (green and red lines in figure 2*c*). Afterwards, radial rays that touch neighbouring segments (red lines in figure 2*c*) are corrected with the neural network in order to account for the occluded part of the bubble. These steps are illustrated in figure 2, and we refer the reader to Hessenkemper *et al.* (2022) for more technical detail. Here, we show in figure 3 the example images of detected bubbles with corrected outline for all the six cases. While the *SmTap*, *LaTap* and *LaPen* cases have mostly irregular bubble shapes associating with shape oscillations, the cases *SmPen*, *SmPen+* and *LaPen+* have fixed shapes. In all of the cases considered, bubble coalescence or breakup was extremely rare and plays a negligible role in the behaviour of the flow. This could be quantified further by computing the Hinze scale for our cases. However, computing this scale requires measuring the turbulent kinetic energy dissipation rate, and this cannot be done reliably using our current experimental set-up.

The bubble size is calculated using the volume-equivalent bubble diameter of a spheroid as $d_p = (d_{maj}^2 d_{min})^{1/3}$, where d_{maj} and d_{min} are the lengths of the major and minor axes of the fitted ellipse, respectively. We observe that the surfactant changes the bubble shape dramatically. For the smaller bubbles with $C_\infty = 1000$, the shape is close to a sphere with a small aspect ratio $\chi = d_{maj}/d_{min} = 1.2$, while for the tap water case, i.e. $C_\infty = 0$, we obtain $\chi = 1.8$. For the larger bubbles, we also have aspect ratios in a similar range, with χ decreasing from 1.8 to 1.3 when going from higher to lower surfactant concentrations.

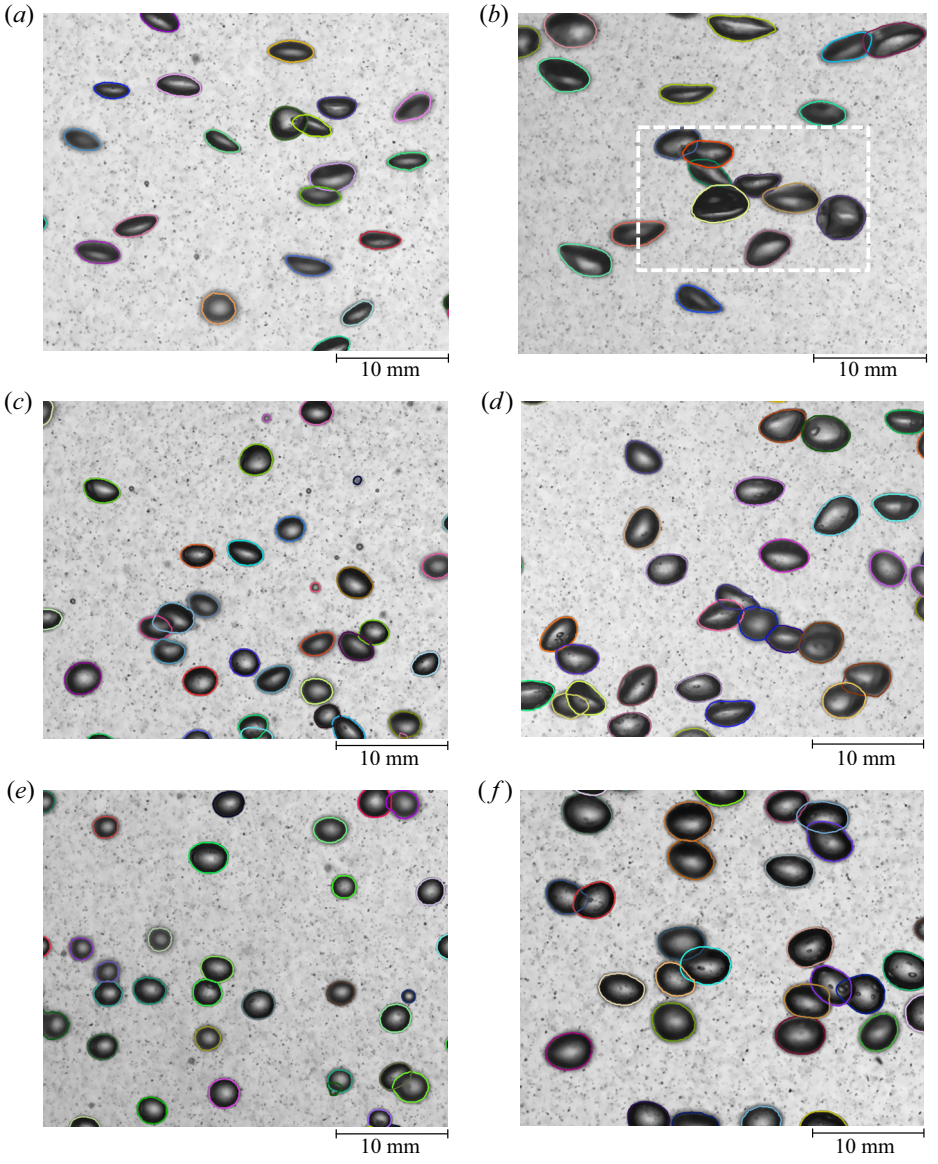

Figure 3. Example images of the bubbles with fitted contours for an arbitrary instant. (*a*,*c*,*e*) Smaller bubbles with (*a*) case *SmTap*, (*c*) case *SmPen* and (*e*) case *SmPen+*. (*b*,*d*,*f*) Larger bubbles with (*b*) case *LaTap*, (*d*) case *LaPen* and (*f*) case *LaPen+*. The area enclosed by the white dashed line in (*b*) corresponds to the region shown in figure 2.

After the bubble detection, the centroids are tracked in each image pair to obtain corresponding bubble velocities. Again, a shallow DoF is used, which allows us to select only sharp bubbles in the column centre by evaluating the grey value derivative along their contour. We choose a grey value derivative threshold that provides a centre region of approximately 15 mm thickness ($3d_p$–$4d_p$) in which the bubbles are evaluated. Some of the important bubble properties are listed in table 1.

It should be noted here that in the case of ellipsoidal bubbles, i.e. the tap water cases, errors in the determined size are larger due to the bubbles being tilted with respect to

the camera. This error can result in a bubble size overprediction of up to 25 % for a strongly tilted spheroidal bubble with fixed shape, which is, however, on average much lower due to the normal distribution of the orientation angle with a maximum approximately zero (Bröder & Sommerfeld 2007). Using the single-bubble data with two cameras (separate experiments reported in § 3.2), we estimate the overprediction of the average volume-equivalent diameter for a fixed spheroidal-shaped bubble (corresponding to case *SmTap*) to be approximately 4 %. Due to the irregular (wobbling) bubble surfaces, the error for the larger bubbles in the *LaTap* case are unknown, but we expect it to be of the same order of magnitude. The error for the void fraction is approximately 5 %–8 % (Hessenkemper *et al.* 2022), and the error of the bubble velocity is approximately 4 %.

3. Surfactant properties and single-bubble behaviour

3.1. *Surfactant properties*

The effect of surfactants on the bubbles arises fundamentally due to their impact on the shear stress at the gas–liquid interface, and depends upon the species of surfactants along with their concentration. The variety of surfactants is huge, and our quantitative understanding of their effect on the base fluid is still in its infancy. There are also sometimes 'untypical' scenarios reported. Ybert & di Meglio (1998) showed the effect of surfactant desorption, leading to a remobilization of the interface by considering bubbles contaminated with sodium dodecyl sulfate (SDS). This surfactant has a significant desorption velocity, and they found that due to the progressive remobilization of the interface, the rise velocity of the SDS-preloaded bubble increases over a large portion of its trajectory (see their figure 12), until reaching a constant value. Similar phenomena were also reported by the same authors (Ybert & di Meglio 2000) for short-chain alcohols, where they illustrated bubble rise velocities in ethanol–water solution that were almost indistinguishable from those in pure water, because of its fast desorption kinetics.

In the present study, we focus on the limit of high bubble Péclet number ($Pe = d_p \, \| \boldsymbol{U}^G \| / D$, where d_p is the bubble diameter, $\boldsymbol{U}^G$ is the averaged bubble velocity, and D is the diffusion coefficient of the surfactant in the liquid), relatively low surfactant concentration compared to the critical micelle concentration (above which surfactants can spontaneously aggregate to form micelles, and the surface tension remains constant) and low rate of desorption. Under these conditions, surface convection is dominant compared to the adsorption–desorption kinetics and diffusive transport of surfactants on the bubble surface. Surfactants collect in a stagnant cap at the back end of the bubble, while the front end is stress-free and mobile. Palaparthi *et al.* (2006) call this the 'stagnant cap regime' – that most commonly realized in typical cases of bubbles moving in a contaminated solution; in this regime, the bubbles are affected significantly by the surfactant, as shown by numerical and experimental results of the rise velocity and wake structure.

In our experiments we use 1-Pentanol as the surfactant and use bulk concentrations $C_\infty = 0$, 333 and 1000 ppm for the six bubble swarm cases. Tests for a single bubble rising in the column were also conducted with concentrations up to 2000 ppm (discussed in § 3.2). Here, the main reason for choosing 1-Pentanol is that with this surfactant (and these concentrations), the bubbles adapt very quickly to the surfactants and no transitions in their motion type appear within the FOV (Tagawa *et al.* 2014).

We measure the surface tension separately with a bubble pressure tensiometer, allowing a dynamic determination of the surface tension. For 1-Pentanol concentration 1000 ppm, using profile analysis tensiometry (Eftekhari *et al.* 2021) we observe a surface tension reduction $\sim$7 % compared to tap water. For $C_\infty = 333$ ppm, the reduction is $\sim$2.3 %,

which we estimate using linear interpolation (valid at these concentrations; see Cheng & Park 2017). The Péclet number is of the order of 10^5, indicating that the convection time scale is very small compared to the time scale of the diffusion on the bubble surface. The solubility for 1-Pentanol is 2500 mol m^{-3}, which is much higher than the present cases (1000 ppm $\sim$9.19 mol m^{-3}). Micelles do not form in the bulk aqueous phase, as indicated by the fact that the bubble terminal velocity remains unchanged when C_∞ is increased further (i.e. no surface remobilization has occurred), to be reported later for a single bubble.

3.2. *Preliminary test for single bubble*

To provide reference cases later for the bubble swarms analysis, we first examine the effect of the surfactants on an isolated bubble in the same set-up by varying the concentration of 1-Pentanol C_∞ with levels 0, 333, 666, 1000, 1500 and 2000 ppm in tap water. This is a wider range than that used for the bubble swarms to check if any interface remobilization occurs at high concentration. We use a single sparger in the column centre, but vary two types of sparger sizes for each C_∞, which are also used for the bubble swarm results to generate (approximately) two bubble sizes. Here, we generate single bubbles continuously by setting a small gas flow rate as we also did in our previous investigation (Hessenkemper *et al.* 2021*a*). The low generation frequency of 1 Hz ensures a large enough distance between successive bubbles to avoid any influence from a leading bubble, but allows us to study multiple same-sized bubbles under the same conditions for better statistics.

For the evaluation of the single-bubble rising trajectory in three-dimensions, we conducted stereoscopic measurements with an additional second camera of the same type placed perpendicular with respect to the imaging direction of the first camera. The single-bubble images are also captured with frame rate 500 f.p.s., but with larger f-stop 11, since sharp bubble outlines at all depth positions are required. As no overlapping bubbles have to be distinguished in the single-bubble experiments, we use a conventional image processing approach here instead of the CNN-based one that is used for bubble swarms. At first, sharp edges marking the outline of the bubbles are detected with a Canny edge detector. The solid of revolution is then used to determine the volume of the bubble by half rotating the left and right halves of the bubble that is split by the vertical rotation centre of a two-dimensional bubble projection. Afterwards, the volumes of the two camera perspectives are averaged to minimize the remaining perspective errors. Further geometric properties, such as the bubble major axis, defined as the largest extent in a two-dimensional projection, and the bubble minor axis, defined as the largest extent perpendicular to the bubble major axis, are also extracted from the bubble projections (Ziegenhein & Lucas 2017). In comparison to the usual approach of fitting ellipses around the contour of detected bubbles, almost the same volume and semi-axis length are obtained, with only minor deviations for irregular-shaped bubbles (Ziegenhein & Lucas 2019). Afterwards, the centroid of the bubble projections is tracked through successive images to obtain time-resolved instantaneous bubble velocities $\tilde{\boldsymbol{u}}^G$, which can be decomposed into a ensemble-averaged part $\boldsymbol{U}^G$ and a fluctuating part $\boldsymbol{u}^G$. The same decomposition is also used for the liquid phase with $\tilde{\boldsymbol{u}}^L = \boldsymbol{U}^L + \boldsymbol{u}^L$ in later sections.

Figure 4(*a*) shows the bubble diameters using two types of sparger size as a function of C_∞. The bubble size is reduced slightly when adding 1-Pentanol for both types of sparger, generating smaller bubbles from 2.9 mm ($C_\infty = 0$ ppm) to 2.7 mm ($C_\infty = 1000$ ppm), and larger bubbles from 4.4 mm ($C_\infty = 0$ ppm) to 4.1 mm ($C_\infty = 1000$ ppm). This is due to the influence of the surfactants that reduce the surface tension and hence affect the bubble formation at the rigid orifice (Loubière & Hébrard 2004; Drenckhan & Saint-Jalmes 2015).

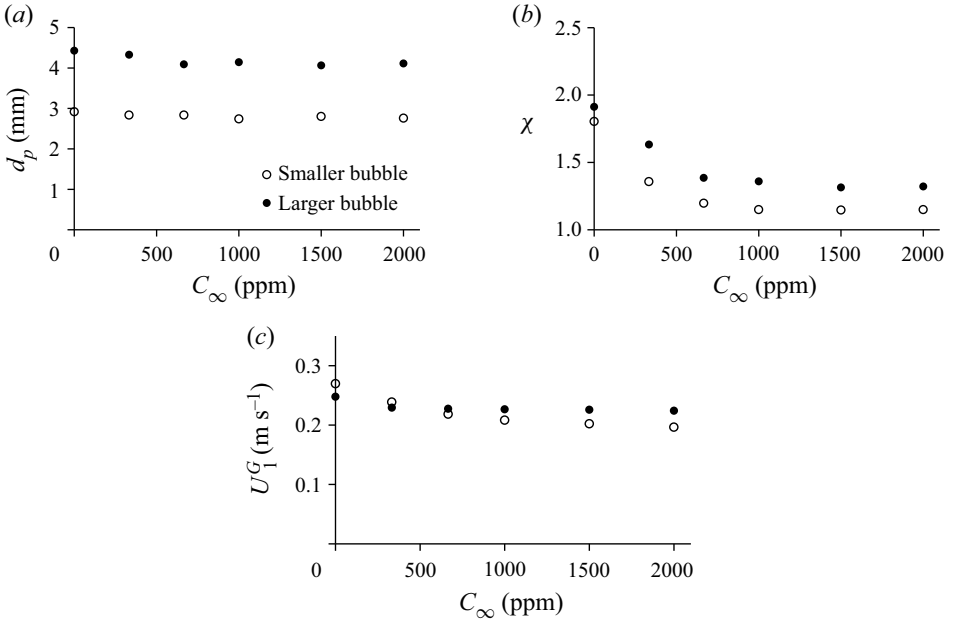

Figure 4. Measured single-bubble (*a*) size, (*b*) aspect ratio and (*c*) rise velocity in different 1-Pentanol concentrations.

A similar trend can also be found in table 1 for the corresponding bubble swarm cases. In contrast to bubble size, the bubble shape changes dramatically (figure 4*b*), with the aspect ratio reducing from 1.8 at 0 ppm to 1.15 at 1000 ppm for the smaller bubble, and 1.9 at 0 ppm to 1.36 at 1000 ppm for the larger bubble. Further increasing C_∞ does not change the bubble shapes for the present smaller and larger bubbles. A similar trend can be found for the averaged rise velocity U_1^G for the both bubble sizes, namely, increasing 1-Pentanol concentration above 1000 ppm does not affect U_1^G. For both bubble sizes and for all concentrations considered, we found no increase of the rise velocity, nor any change in terms of aspect ratio above $C_\infty = 1000$ ppm, hence no surface remobilization has occurred. Based on these, we assume that for both bubble sizes, a saturated contamination state (at least from the hydrodynamic perspective) is reached at the threshold $C_\infty \approx 1000$ ppm.

We now look more in detail at the single-bubble cases with $C_\infty = 0$, 333 and 1000 ppm, since they have the same set of C_∞ values as the swarm cases that we will discuss later. We label these cases *S-SmTap*, *S-SmPen* and *S-SmPen+* for the smaller bubble, and *S-LaTap*, *S-LaPen* and *S-LaPen+* for the larger bubble, respectively (where the first letter *S* denotes a single bubble). Figure 5(*a*) shows a three-dimensional view of the bubble trajectories for the three smaller bubble cases, while figure 5(*b*) shows a view of these trajectories from the top. The trajectories are similar to those found by Tagawa *et al.* (2014) for 2 mm bubbles, with helical trajectories at lower 1-Pentanol concentration (see *S-SmTap* and *S-SmPen*), and zigzag rising paths for higher concentration (*S-SmPen+*). These zigzag and helical motions are accompanied by oscillations in the vertical velocity $\tilde{u}_1^G$ plot of figure 5(*c*) (corresponding to the paths in figure 5*a*), i.e. the bubbles alternately speed up and slow down as they rise. As expected, the *S-SmPen+* case has much higher oscillation in $\tilde{u}_1^G$, compared to the *S-SmTap* and *S-SmPen* cases. This is caused by the relatively unstable wake structure that is associated with zigzag paths, rather than the more

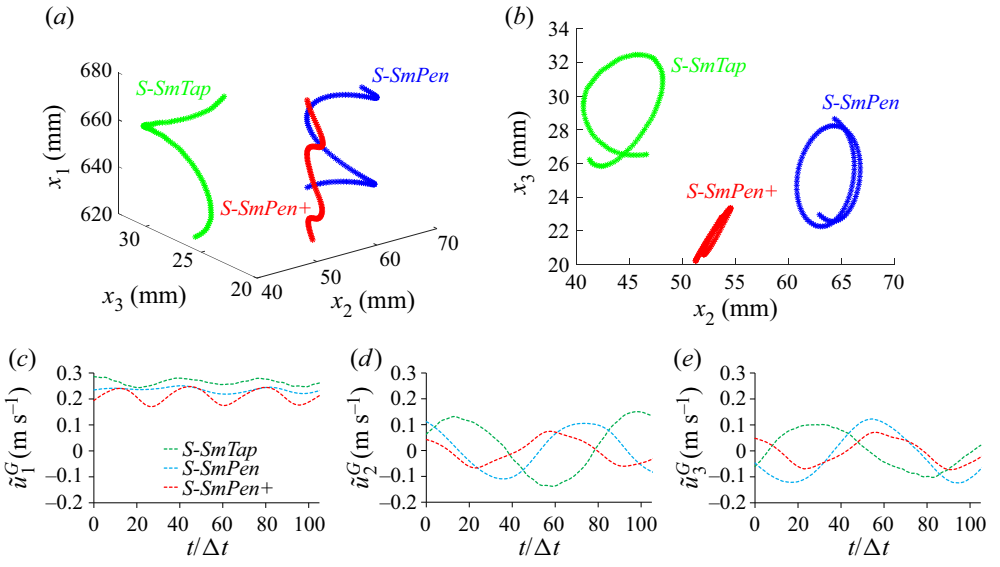

Figure 5. (*a*) Three-dimensional trajectories and (*b*) their top view, and corresponding instantaneous bubble velocities with components (*c*) $\tilde{u}_1^G$, (*d*) $\tilde{u}_2^G$ and (*e*) $\tilde{u}_3^G$ over time (normalized by $\Delta t = 2$ ms) of smaller single bubbles at $C_\infty = 0$ ppm (*S-SmTap*), $C_\infty = 333$ ppm (*S-SmPen*) and $C_\infty = 1000$ ppm (*S-SmPen+*). All plots are from the same track of the particular case.

stable one associated with the helical trajectories (Cano-Lozano *et al.* 2016). Moreover, we observe that the helical trajectories of *S-SmTap* and *S-SmPen* are not as regular as those in Tagawa *et al.* (2014) due to our larger bubble size ∼3 mm. This is also indicated by the vertical velocities (figure 5*c*), showing oscillations in *S-SmTap* and *S-SmPen* compared to the constant $\tilde{u}_1^G$ for the cases with relatively perfect helical rising paths in Tagawa *et al.* (2014). The characteristic diameters of the helical paths in both cases are close to 10 mm, which is similar to that found in Riboux *et al.* (2010) for a 2.5 mm bubble rising in tap water. This characteristic diameter is much smaller than the depth of the present column, so the side-wall effects are negligible in the experiment.

Another important observation from figures 5(*c–e*) is that the frequency of the vertical velocity is approximately twice as large as that of the horizontal velocities due to the frequency of the force oscillations in the corresponding directions (Mougin & Magnaudet 2006). Moreover, there is a trend that with increasing C_∞, the frequency of the oscillation in velocities increases. This is in line with the observation reported in Tagawa *et al.* (2014) for their smaller bubbles.

In figure 6, we plot the same quantities for the three larger bubble cases. A fixed path type cannot be found for case *S-LaTap*. Although in figure 6(*e*) it shows a zigzagging trend, there are many other snapshots showing a flattened helix (not shown here). Case *S-LaTap* belongs to the chaotic regime due to the very large Re_p and Eo, while *S-LaPen* exhibits a flattened helical motion, and *S-LaPen+* converges towards a zigzag path. Moreover, compared to the smaller bubbles, the vertical velocities (figure 6*a*) in all three larger bubble cases display irregular oscillations.

4. Flow characterization for bubble swarm

Basic statistics of both phases for the considered cases are plotted in figure 7. Both the void fraction (figure 7*a*) and the vertical gas/liquid velocity (figure 7*b*) have very flat profiles,

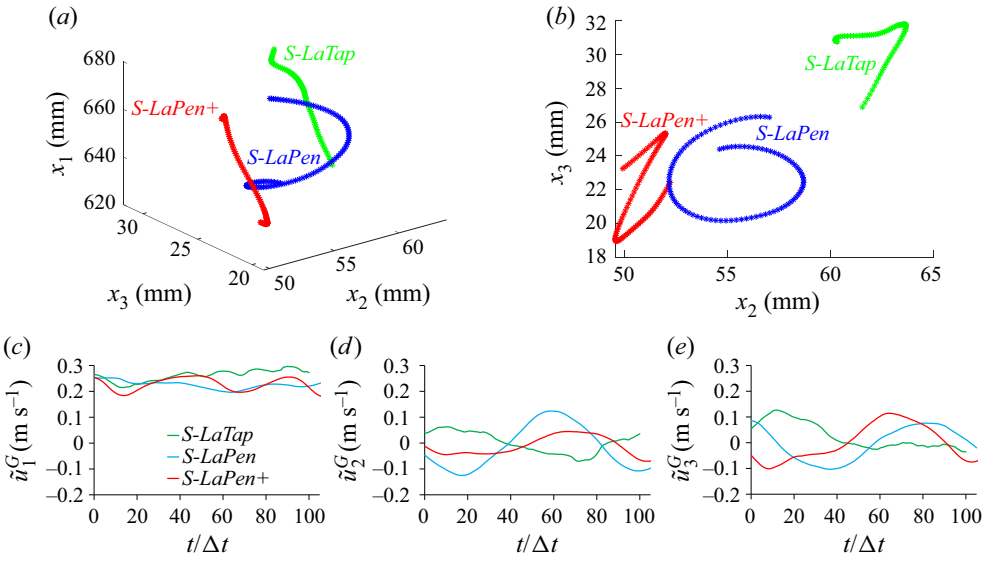

Figure 6. (*a*) Three-dimensional trajectories and (*b*) their top view, and corresponding instantaneous bubble velocities with components (*c*) $\tilde{u}_1^G$, (*d*) $\tilde{u}_2^G$ and (*e*) $\tilde{u}_3^G$ over time (normalized by $\Delta t = 2$ ms) of larger single bubbles at $C_\infty = 0$ ppm (*S-LaTap*), $C_\infty = 333$ ppm (*S-LaPen*) and $C_\infty = 1000$ ppm (*S-LaPen+*). All plots are from the same track of the particular case.

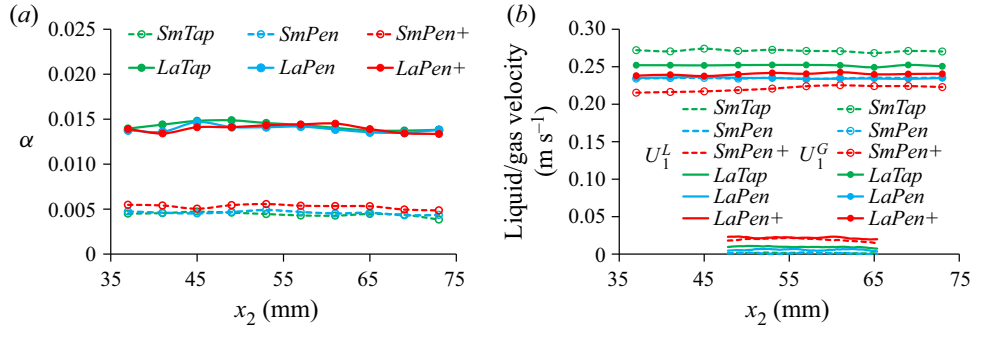

Figure 7. (*a*) Gas void fraction and (*b*) liquid/gas vertical velocity along the horizontal axis of the FOV.

indicating statistical homogeneity of the current flow in the FOV. Even with zero bulk flow (averaged over the entire flow cross-section), we observe for almost all the cases $U_1^L \neq 0$ along the horizontal axis of the FOV (especially for the cases *SmPen+* and *LaPen+*), so that the relative velocity in the FOV is in general not equal to the bubble terminal rise velocity. Furthermore, due to the Marangoni effect, we find that the bubble swarms rise more slowly with increasing C_∞ for both smaller and larger bubbles, consistent with our results for the corresponding single bubble in § 3.2. It is worth noting that although *LaPen* and *LaPen+* have a similar U_1^G, *LaPen+* has a smaller relative velocity due to the higher U_1^L, as indicated by its smaller bubble Reynolds number (table 1).

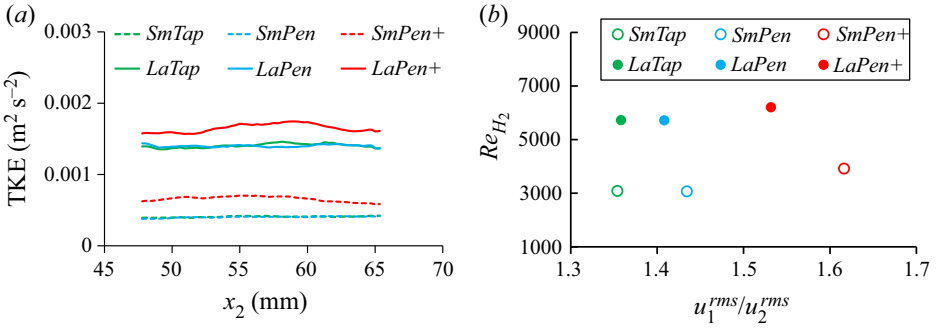

Figure 8. (*a*) Turbulent kinetic energy along the horizontal axis of the FOV. (*b*) Reynolds number Re_{H_2} plotted versus large-scale anisotropy ratio u_1^{rms}/u_2^{rms}.

We now turn to consider the role played by the surfactant in generating BIT. Hereafter, all average quantities refer to the liquid, so that the upper index L is dropped for simplicity. In figure 8(*a*), we plot the turbulent kinetic energy (TKE) k, calculated as

$$k = \tfrac{1}{2}\left((u_1^{rms})^2 + 2(u_2^{rms})^2\right), \tag{4.1}$$

assuming that the out-of-plane velocity variance is equal to the measured horizontal component. This approximation – axisymmetry about the vertical direction – is expected for the BIT dominated flows far from the wall. Here, u_1^{rms} and u_2^{rms} are the root-mean-square values of the vertical and horizontal velocity fluctuations, respectively. For both smaller and larger bubbles, surprisingly, the TKE is highest for the cases with the highest C_∞, although *SmPen+* and *LaPen+* have the lowest Re_p in the cases of smaller and larger bubbles, respectively. It is also interesting to note that TKE in the cases *SmPen* and *LaPen* does not change much compared to *SmTap* and *LaTap*, respectively, indicating that the amount of 1-Pentanol added ($C_\infty = 333$ ppm) is not enough to modify the BIT already initiated in the tap water system. However, we should keep in mind that the bubble sizes in *SmPen* and *LaPen* are slightly smaller than their corresponding tap water cases (see table 1), so that if the TKE is almost the same for the $C_\infty = 0$ and $C_\infty = 333$ ppm cases, then the surfactant is in fact leading to a positive contribution to the BIT generation.

In table 2, we summarize the effect of the surfactant on three aspects that influence BIT. Aside from reducing the bubble Reynolds number, the bubble surface instability (e.g. deformation and wobbling) also reduces when increasing C_∞, and both of these reductions have a negative impact on BIT production. This suggests that the change of boundary condition induced by increasing C_∞ plays the key role in causing the TKE to be enhanced by the addition of surfactants. Following our previous study (Ma *et al.* 2021), we define a Reynolds number $Re_{H_2} \equiv u^* H_2/\nu$, indicating the range of scales in the turbulent bubbly flows. Here, $u^* \equiv \sqrt{(2/3)k_{FOV}}$, and k_{FOV} is the TKE averaged over the FOV of the liquid phase. In figure 8(*b*), we depict Re_{H_2} versus the large-scale anisotropy ratio u_1^{rms}/u_2^{rms} (also averaged over the FOV). The figure reflects the same behaviour as the TKE, namely the case with the highest C_∞ also has the largest Re_{H_2} for the corresponding bubble size group. Furthermore, we find that for large scales whose fluctuating velocities are characterized by u_1^{rms} and u_2^{rms}, the smaller bubbles produce more anisotropy in the flow than the larger bubbles, as reflected by a larger ratio u_1^{rms}/u_2^{rms} for the cases *SmTap*, *SmPen* and *SmPen+*. This is in very close agreement with our previous study based on DNS data of bubble-laden

Factor influencing BIT	Change by increasing C_∞	Contribution to BIT
Bubble Reynolds number	reduced 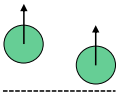	−
Boundary condition	free-slip ⟶ no-slip 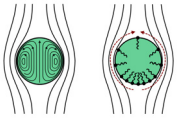	+
Surface instability (deformation, wobbling, etc.)	reduced 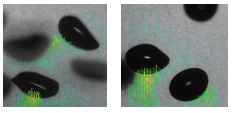	−

Table 2. Summary of how surfactants modify the bubble Reynolds number, boundary condition and deformability, and the impact (positive or negative) that these modifications will have on the intensity of the turbulence generated by the rising bubbles. The right-hand image in the centre column is a schematic representation of surfactant distribution on the surface of a rising bubble, and the red dashed arrows indicate the Marangoni stress.

turbulent channel flow driven by a vertical pressure gradient and with no-slip boundary conditions on the bubble surfaces (Ma *et al.* 2021).

The more important point prompted by figure 8(*b*) is that the large-scale anisotropy increases significantly with increasing surfactant concentration for both smaller and larger bubbles. This behaviour is due to the effect of the surfactant on both the wake structure and trajectory type of the bubbles as C_∞ changes, as was already seen for different single bubbles in figures 5 and 6. Indeed, these anisotropy results indicate that the increase of TKE due to the addition of surfactants is due mainly to the change of the bubble surface boundary properties, and not due to an increase of the lateral movement, since the results indicate that the lateral motions become weaker compared with the vertical motions as the surfactant concentration is increased. This is in contrast to the case of single buoyant or heavy particles that are rising/settling in liquids where enhanced horizontal motion was found to be the cause of increased liquid velocity fluctuations despite there being a corresponding reduction in particle Reynolds number (Veldhuis, Biesheuvel & Lohse 2009; Horowitz & Williamson 2010; Mathai *et al.* 2018).

In figure 9, the PDFs of the liquid velocity fluctuations (normalized by their standard deviations) are shown for both directions. In agreement with the previous experimental results (Riboux *et al.* 2010; Lai & Socolofsky 2019), we find that the PDFs of the vertical velocity fluctuations are strongly positively skewed for all the cases, while the PDFs of the horizontal velocities are symmetric. We also find that for the three smaller bubble cases, the PDFs become increasingly non-Gaussian in the order *SmPen+*, *SmPen*, *SmTap*, which corresponds to decreasing C_∞ (1-Pentanol) and Re_{H_2}. By contrast, for the larger bubble cases, the dependence of the PDFs on C_∞ is very weak. Explanations for the observed behaviour will be considered in the next section.

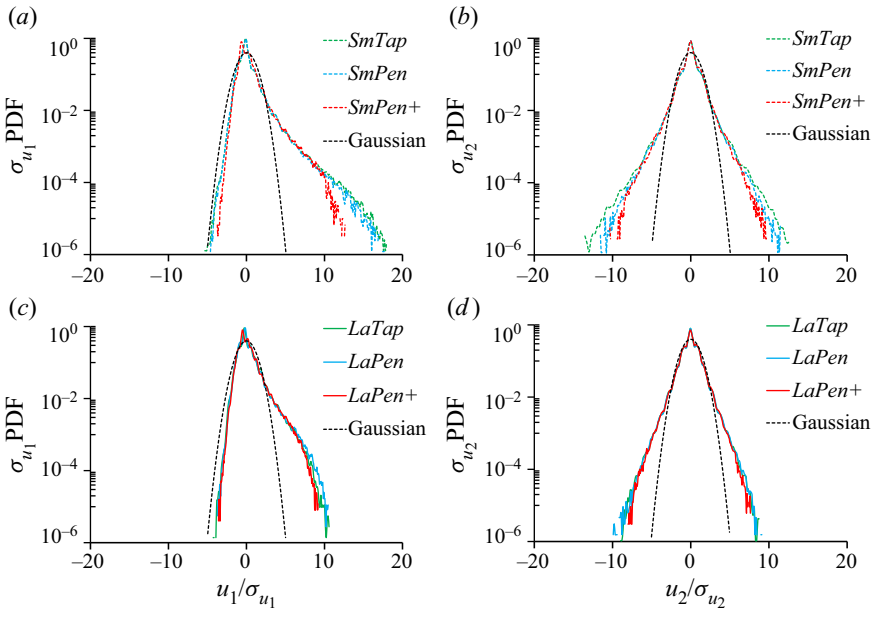

Figure 9. Normalized PDFs of liquid velocity fluctuations: (*a*,*b*) the three smaller bubble cases, and (*c*,*d*) the three larger bubble cases.

5. Turbulence modification across scales

5.1. *Turbulence anisotropy*

The components of the second-order velocity structure function are defined as

$$D_2^{ij}(\boldsymbol{x}, \boldsymbol{r}, t) \equiv \langle \Delta u_i(\boldsymbol{x}, \boldsymbol{r}, t)\, \Delta u_j(\boldsymbol{x}, \boldsymbol{r}, t) \rangle, \tag{5.1}$$

where $\Delta u_i(\boldsymbol{x}, \boldsymbol{r}, t)$ denotes the difference in the velocity at positions $\boldsymbol{x}$ and $\boldsymbol{x} + \boldsymbol{r}$ at time t, and $\langle \cdot \rangle$ denotes an ensemble average. Hereafter, we suppress the space $\boldsymbol{x}$ and time t arguments since we are considering a flow that is statistically homogeneous and stationary over the FOV. The calculation of liquid velocity increments in a bubbly flow is somewhat delicate, since the liquid velocity is not defined at points occupied by a bubble. To overcome this non-continuous velocity signal challenge, the statistics of the velocity increments were computed based only on lines of grid points spanning the FOV at time instants where none of the points on the line were occupied by a bubble. A more detailed discussion of this method can be found in Ma *et al.* (2021, 2022).

The PSV measurement provides access to data associated with separations along two directions, namely, the vertical separation $\boldsymbol{r} = r_1 \boldsymbol{e}_1$ ($r_1 = \|\boldsymbol{r}\|$) and the horizontal separation $\boldsymbol{r} = r_2 \boldsymbol{e}_2$ ($r_2 = \|\boldsymbol{r}\|$). Hence we are able to compute the four contributions $D_2^L(r_1) = D_2^{11}(r_1)$, $D_2^L(r_2) = D_2^{22}(r_2)$, $D_2^T(r_1) = D_2^{22}(r_1)$ and $D_2^T(r_2) = D_2^{11}(r_2)$ based on the Cartesian coordinate system depicted in figure 1.

Figures 10(*a*) and 10(*b*) show the measured transverse and longitudinal second-order structure functions of the u_1 component, respectively. The results show that the values of the structure functions increase in the order *SmTap*, *SmPen*, *SmPen+*, *LaTap*, *LaPen*, *LaPen+*, which corresponds to larger bubble size and higher surfactant concentration. This ordering also holds for the u_2 component computed (not shown). Similar to the results for the TKE, while the difference between *Sm(La)Tap* and *Sm(La)Pen* is small, $D_2^{\gamma\gamma}$ (no index

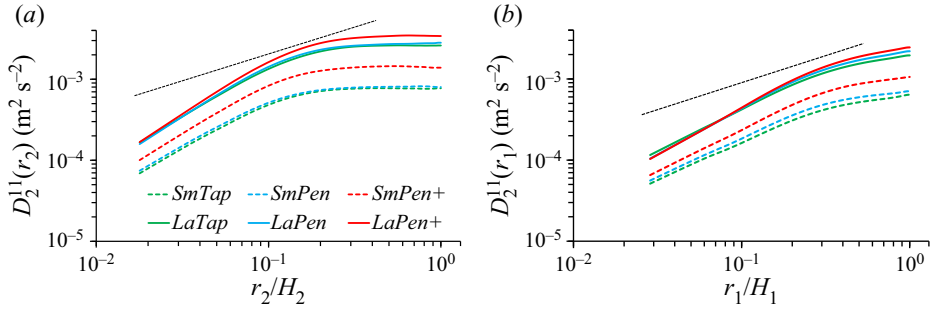

Figure 10. (*a*) Transverse and (*b*) longitudinal second-order structure functions of the u_1 component, with separations along the (*a*) horizontal and (*b*) vertical directions. The black dashed lines indicate slope $r^{2/3}$.

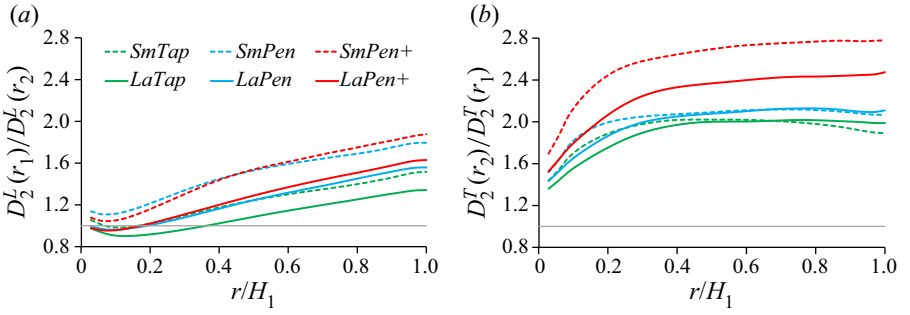

Figure 11. Ratio of (*a*) longitudinal and (*b*) transverse structure functions in different separation directions for all the cases. The horizontal lines indicate the value unity.

summation is implied for γ) for *Sm(La)Pen+* have noticeably higher values across most scales for both smaller and larger bubble sizes. The plot shows the $r^{2/3}$ scaling that would be expected for single-phase HIT according to Kolmogorov's 1941 theory (Pope 2000). The results show that for the bubbly turbulent flows in our experiments, an extended $r^{2/3}$ scaling regime does not occur in any range of separations. At smaller separations, the structure functions exhibit behaviour consistent with a dissipation range, e.g. $D_2^{11}(r_1) \propto r_1^2$. However, our experimental resolution is not fine enough to determine whether this really does correspond to dissipation range scaling, or whether this scaling is caused by other effects in the flow (including the frequency of wake oscillations), and that the true dissipation range occurs at separations smaller than we can resolve. Moreover, since there is no inertial range in the flow, there is no way to estimate the energy dissipation rate based indirectly on the structure functions, as is often done in other contexts.

To characterize the multiscale anisotropy associated with D_2^{ij}, we plot the ratios of components $D_2^L(r_1)/D_2^L(r_2)$ and $D_2^T(r_2)/D_2^T(r_1)$ in figure 11, which would be equal to unity for an isotropic flow (Carter & Coletti 2017). Generally, the results show that both ratios decrease monotonically for decreasing separation. Moreover, the ratio of the transverse structure functions departs more strongly from unity than the longitudinal ones. By comparing the cases with the same bubble size, we find that generally the cases with higher surfactant concentration generate stronger anisotropy in the flow across the scales, and this trend is most obvious in the plot for $D_2^T(r_2)/D_2^T(r_1)$. This is in agreement with the results of the large-scale anisotropy in § 4.

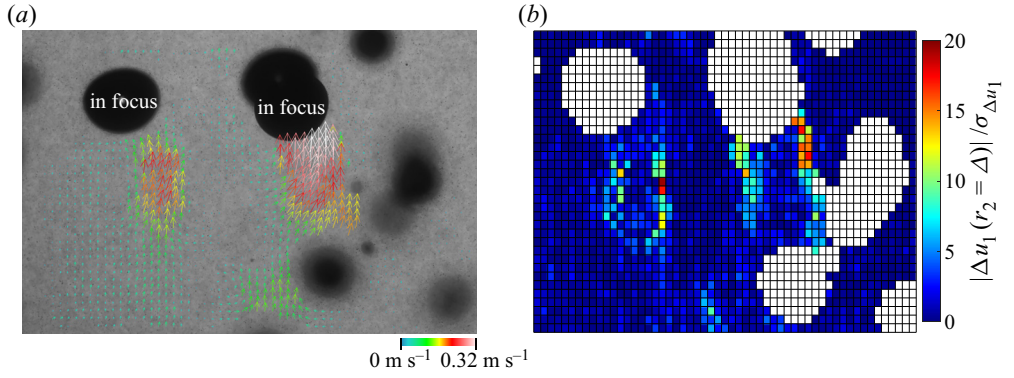

Figure 12. (*a*) Snapshot of the original velocity vector. (*b*) Intensity distributions of the normalized velocity increment $|\Delta u_1(r_2 = \Delta)|/\sigma_{\Delta u_1}$ from the same instant based on the *SmPen+* case. The in-focus bubbles are denoted in (*a*).

Furthermore, considering the cases with the same C_∞, our results indicate that smaller bubbles generate stronger anisotropy in the flow, consistent with our previous studies (Ma *et al.* 2021, 2022) that considered only fully contaminated bubbles. However, the results in figure 11 show that it is not true in general that smaller bubbles generate stronger anisotropy in the flow, because it depends on the surfactant concentration. For example, figure 11 shows that *LaPen+* can be more anisotropic than *SmTap*.

5.2. *Extreme fluctuations in the flow*

Having explored the role of surfactants on the flow anisotropy, we now turn to consider the effect of surfactants on extreme fluctuations of the velocity increments – a phenomenon associated with internal intermittency in single-phase turbulence (Frisch 1995; Sreenivasan & Antonia 1997). In the present bubbly flows, extreme events in the liquid phase result from the boundary of the wakes produced by the bubbles (Ma *et al.* 2022). These contributions can be seen in figure 12, with the normalized velocity increments ($r_2 = \Delta$, where Δ is one PSV grid) showing large values at the edge of the wakes, while the velocities are largest inside the wakes. Another possible contribution to extreme events would come from the flow in the boundary layer at the top of the rising bubble where the flow may change abruptly from being equal to the bubble surface velocity to the background bulk velocity over a thin boundary layer. For spherical bubbles with large Re_p rising in a quiescent flow, the thickness of this boundary layer is $O(d_p\, Re_p^{-1/2})$ (Moore 1963; Batchelor 1967). However, we cannot resolve the velocity fluctuations in this thin boundary layer with our current experimental method (and the results discussed below should be interpreted accordingly), and further work is needed to understand how these regions might contribute to extreme fluctuations in the flow.

In figure 13, we plot the PDFs of the velocity increments for separations equal to ten PSV grids ($r = 10\Delta = 0.18H_2$), corresponding to an 'eddy size' with $O(d_p)$. (The results for other separations show qualitatively similar trends and so are not shown.) First, all of the six cases show that the velocity increments have strongly non-Gaussian PDFs, just as in single-phase turbulence. Second, while the PDFs of the transverse velocity increments in figures 13(*c*,*d*) are almost symmetric, the PDFs of the longitudinal velocity increments in figures 13(*a*,*b*) are negatively skewed for the horizontal separations r_2. Finally, with respect to the effect of bubble size and surfactant concentration, the results

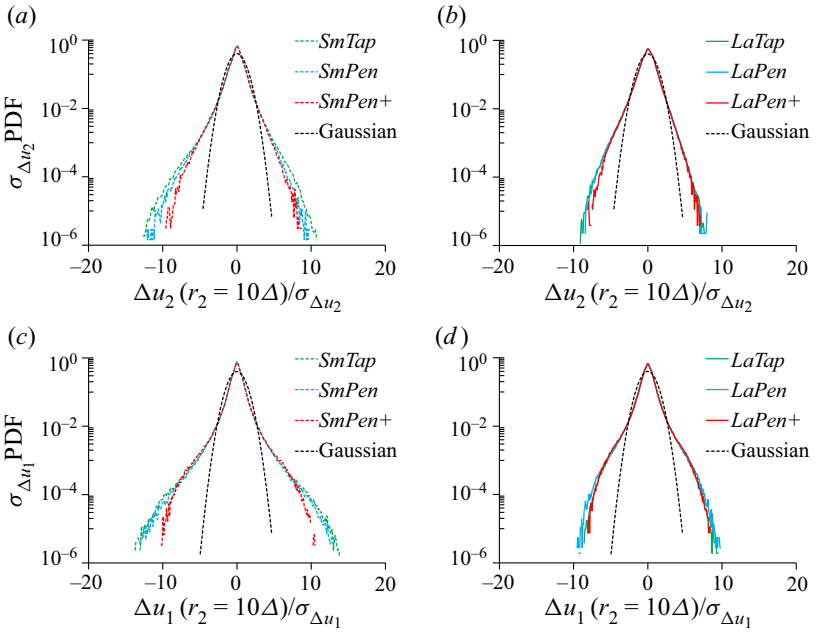

Figure 13. Normalized PDFs of the (*a*,*b*) longitudinal and (*c*,*d*) transverse velocity increments for (*a*,*c*) the three smaller bubble cases and (*b*,*d*) three larger bubble cases, with the separations along the horizontal direction ($r_2 = 10\Delta$, where Δ is one PSV grid).

show very interesting behaviours: for the smaller bubbles, both the longitudinal and transverse PDFs (figures 13*a*,*c*) become increasingly non-Gaussian in the order *SmPen+*, *SmPen*, *SmTap*, which corresponds to the order of decreasing C_∞ of 1-Pentanol. This is consistent with our previous finding (Ma *et al.* 2022) that the non-Gaussianity of the PDFs of the velocity increments becomes stronger as the Reynolds number (here, Re_{H_2}) is decreased in bubble-laden turbulent flow considered here, while the opposite occurs for single-phase turbulence (Frisch 1995). An explanation for why the intermittency is largest for the cases with lower surfactant concentration can be given as follows. For these three cases, the volume fraction is not large, and there are relatively few regions in the flow where turbulence is produced due to the bubble wakes, meaning that turbulence in the flow is very patchy and therefore intermittent. For the cases with higher C_∞, they have larger flow Reynolds numbers accompanied by longer and wider bubble wakes. As a result, the wake regions are more space filling and hence the flow is less intermittent than the cases with lower surfactant concentration, which have shorter and narrower bubble wakes. Again, this difference compared to intermittency in single-phase turbulence can be traced back to the fact that the regions of intense small-scale velocity increments occur near the turbulent/non-turbulent interface at the boundary of the bubble wake, which is more similar to so-called external intermittency (Townsend 1949) than internal intermittency.

The C_∞ dependency of the small-scale intermittency just discussed for the smaller bubbles is, however, much weaker for the larger bubbles (figures 13*b*,*d*). A potential reason for this difference is that the three larger bubble cases have volume fractions that are almost three times larger than those for the smaller bubbles, and the bubble wake volume is also much larger, with much higher turbulence intensity generated by the wakes. As a result of these properties, while there are significant regions of the flow that are almost quiescent

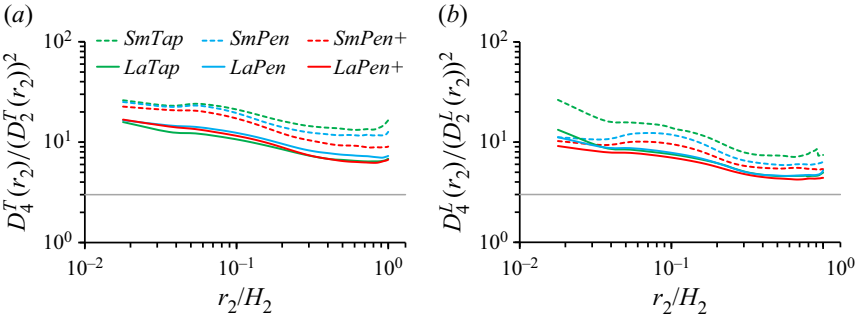

Figure 14. Normalized fourth-order (*a*) transverse and (*b*) longitudinal structure functions, corresponding to the kurtosis of the velocity increments along the horizontal direction. The horizontal lines indicate the Gaussian value of 3 for the kurtosis.

for the smaller bubble cases, the same is not true for the larger bubbles, with turbulent activity filling a significant fraction of the flow. Due to this, the velocity difference in and outside the wake is smaller for the larger bubble cases than the smaller bubble cases, and the intermittency is less dependent on C_∞ since even for the largest C_∞ case, these velocity differences across the wake boundaries are already smaller. This then explains why *LaTap*, *LaPen* and *LaPen+* do not show the same C_∞ dependence in the PDFs as the smaller bubble cases.

While the PDF results present the effect of the surfactants on the extreme events at a fixed separation, we look at now this property across all the scales quantified by the kurtosis $D_4^T(r_2)/(D_2^T(r_2))^2$ and $D_4^L(r_2)/(D_2^L(r_2))^2$ (figure 14). The first observation from the results in figure 14 is that all six bubble-laden cases show a similar behaviour as r increases, with values of up to 30 gradually reducing as r increases. However, there is still considerable deviation from the Gaussian value of 3 even at the largest scale $r_2/H_2 = 1$. For both the transverse and longitudinal components, the kurtosis is larger for the cases with smaller bubbles, reflecting the same trend as the PDFs of the velocity increments at the single scale $r_2 = 10\Delta$ (see figures 13(*a*,*b*) or 13(*c*,*d*)). The qualitative effect of the surfactant concentration on the extreme events as quantified by the PDF results for $\Delta\boldsymbol{u}(r_2 = 10\Delta)$ (figure 13) can be extended to almost all the scales. While the kurtosis decreases in the sequence *SmTap*, *SmPen* to *SmPen+* across the scales of the flow, the values of the three cases with larger bubbles are very similar.

In table 3, we show the values of the kurtosis of u_1 and u_2 as well as those of Δu_1 and Δu_2 at large separations in order to understand how the non-Gaussianity of the velocity increments relates to the non-Gaussianity of the velocity fluctuations observed in figure 9. Since the largest separations that we can observe are constrained by the FOV, we also compute the theoretical values of the kurtosis of Δu_1 and Δu_2 at infinite separation, assuming that the flow is homogeneous. These theoretical expressions are evaluated from the definitions of the structure functions using the fact that at infinite separations, the velocities at two points are uncorrelated. The resulting expressions are

$$\lim_{r_2/H_2\to\infty} \frac{D_4^T(r_2)}{[D_2^T(r_2)]^2} = \frac{1}{2}\frac{\langle u_1^4\rangle}{\langle u_1^2\rangle^2} + \frac{3}{2}, \tag{5.2}$$

$$\lim_{r_2/H_2\to\infty} \frac{D_4^L(r_2)}{[D_2^L(r_2)]^2} = \frac{1}{2}\frac{\langle u_2^4\rangle}{\langle u_2^2\rangle^2} + \frac{3}{2}. \tag{5.3}$$

Parameter	*SmTap*	*SmPen*	*SmPen+*	*LaTap*	*LaPen*	*LaPen+*
Kurtosis of u_1	23.3	19.8	14.6	9.7	11.2	9.2
Kurtosis of Δu_1 at $r_2/H_2 \approx 1$	13.4	11.7	8.9	6.4	7.1	6.2
Theoretical kurtosis of Δu_1 as $r_2/H_2 \to \infty$	13.2	11.4	8.8	6.4	7.1	6.1
Kurtosis of u_2	11.5	9.0	7.8	6.1	6.2	5.6
Kurtosis of Δu_2 at $r_2/H_2 \approx 1$	7.7	6.0	5.4	4.6	4.7	4.3
Theoretical kurtosis of Δu_2 as $r_2/H_2 \to \infty$	7.3	6.0	5.4	4.6	4.6	4.3

Table 3. Comparison between the kurtosis of the fluctuating velocity and the kurtosis of the velocity increment at large scale. Also shown is the theoretical kurtosis of the velocity increment, which is the value the kurtosis would have at infinite separation in a homogeneous flow.

If u_1 and u_2 have Gaussian distributions, then the kurtosis of u_1 and u_2 is equal to 3, as is the kurtosis of Δu_1 and Δu_2 at $r_2/H_2 \to \infty$. However, for non-Gaussian u_1 and u_2, the kurtosis values for u_1 and u_2 are not equal to those for Δu_1 and Δu_2 at $r_2/H_2 \to \infty$.

The values of the kurtosis of u_1 and u_2 in table 3 reflect the same trend as those based on the velocity increments: the values are larger for smaller bubbles, and decrease in the sequence *SmTap*, *SmPen* to *SmPen+*, while the kurtosis values for *LaTap*, *LaPen* and *LaPen+* are similar. The values of the kurtosis of Δu_1 and Δu_2 measured at $r_2/H_2 \approx 1$ are very close to the theoretical values, indicating that our FOV is sufficiently large to capture the largest scales of the flow.

Finally, in our previous work (Ma *et al.* 2022), we noted that the PDFs of the velocity increments at $r_2/H_2 \approx 1$ are very different from the PDFs of the velocities. This seemed surprising given the expectation that these two PDFs should converge at sufficiently large separations because the correlation of the velocity between the two points vanishes in that limit. We speculated that the lack of convergence of the PDFs was due to our FOV being too small to observe the asymptotic approach of the PDFs at sufficiently large separations. However, the results in (5.2) and (5.3) indicate that our previous expectation of the convergence of these PDFs was in fact mistaken. Indeed, a calculation of other moments shows that more generally, the moments of the velocity increments at large separations will not approach the moments of the velocities unless the velocity fluctuations are Gaussian. Hence it follows that their PDFs will also not approach unless the velocity fluctuations are Gaussian.

6. Conclusions

In this work, we have used experiments to investigate the effect of surfactants on BIT using recently developed PSV and bubble identification techniques for bubble/particle-laden flows. The experiments consider two bubble sizes, 3 and 4 mm, and three different surfactant (1-Pentanol) concentrations for each bubble size. The addition of surfactants changes the bubble shape, as well as the interface boundary condition from a quasi-free-slip condition to a no-slip condition.

To provide some reference cases, we first investigated how 1-Pentanol influences single bubbles in terms of the size of the bubbles formed in the system, the bubble aspect ratios, the bubble rise velocity and the nature of their trajectories. We find that for the two bubble sizes considered, an approximately saturated contamination state is reached at $C_\infty \approx$ 1000 ppm. The effect of the surfactant on the bubble trajectories is similar to that observed in Tagawa *et al.* (2014), with helical trajectories at lower 1-Pentanol concentrations and zigzag rising trajectories for higher concentration for smaller bubble cases. The effect of

the surfactant was similar for the larger bubbles, although in the absence of the surfactants, the trajectories of the larger bubbles appear chaotic.

Our results for bubble swarms show that for BIT-dominated flows, the level of anisotropy is strong in general, and not negligible even at small scales in the flow, consistent with previous results. However, our results reveal that for the same bubble size, the flow anisotropy can be strongly enhanced by increasing the surfactant concentration. We also investigated extreme events in the flow by considering the normalized PDFs of the velocity increments at the scale of the bubble size. For the smaller bubbles, the PDFs become increasingly non-Gaussian when the surfactant concentration is decreased. This is consistent with our previous finding that the non-Gaussianity of the PDFs of the velocity increments becomes stronger as the Reynolds number is decreased in the bubble-laden turbulent flows considered here, the opposite of what occurs for internal intermittency for single-phase turbulence, which increases with increasing Reynolds number. However, the dependency of the non-Gaussianity of the velocity increments on the surfactant concentration is much weaker for the cases with larger bubbles. An explanation for this difference is that the larger bubble cases have much larger volume fractions compared to those for the smaller bubbles, and the bubble wake volume is also much larger, with much higher turbulence intensity generated by the wakes. Due to this, the velocity difference in and outside the wake is smaller for the larger bubble cases than the smaller bubble cases, and the intermittency is less dependent on the surfactant concentration.

While this study has focused on the impact of surfactants on the properties of the liquid turbulence in BIT, another important topic is to investigate how the surfactants impact the bubble clusters and bubble dispersion. These will be investigated in a future study.

Acknowledgements. The authors would like to acknowledge T. Ziegenhein for much technical support in the experimental method over the years. T.M. benefited from fruitful discussions on this topic with J. Fröhlich, Y. Liao, P. Shi, S. Heitkam, K. Schwarzenberger, X. Xu, Y. Tagawa and G. Katul.

Declaration of interests. The authors report no conflict of interest.

Data availability. The data that support the findings of this study are available from T.M. on request.

Author ORCIDs.
Tian Ma https://orcid.org/0000-0002-8406-4698;
Hendrik Hessenkemper https://orcid.org/0000-0002-2588-694X;
Andrew D. Bragg https://orcid.org/0000-0001-7068-8048.

References

Ahmed, Z., Izbassarov, D., Lu, J., Tryggvason, G., Muradoglu, M. & Tammisola, O. 2020 Effects of soluble surfactant on lateral migration of a bubble in a pressure driven channel flow. *Intl J. Multiphase Flow* **126**, 103251.

Atasi, O., Ravisankar, M., Legendre, D. & Zenit, R. 2023 The presence of surfactants controls the stability of bubble chains in carbonated drinks. *Phys. Rev. Fluids* **8**, 053601.

Bachhuber, C. & Sanford, C. 1974 The rise of small bubbles in water. *J. Appl. Phys.* **45** (6), 2567–2569.

Batchelor, G.K. 1967 *An Introduction to Fluid Dynamics*. Cambridge University Press.

Bel Fdhila, R. & Duineveld, P.C. 1996 The effect of surfactant on the rise of a spherical bubble at high Reynolds and Péclet numbers. *Phys. Fluids* **8** (2), 310–321.

Biferale, L., Perlekar, P., Sbragaglia, M. & Toschi, F. 2012 Convection in multiphase fluid flows using lattice Boltzmann methods. *Phys. Rev. Lett.* **108** (10), 104502.

Blaauw, L.J., Lohse, D. & Huisman, S.G. 2023 Sodium chloride inhibits effective bubbly drag reduction in turbulent bubbly Taylor–Couette flows. *Phil. Trans. R. Soc.* A **381** (2243), 20220127.

Bröder, D. & Sommerfeld, M. 2007 Planar shadow image velocimetry for the analysis of the hydrodynamics in bubbly flows. *Meas. Sci. Technol.* **18** (8), 2513.

CANO-LOZANO, J.C., MARTINEZ-BAZAN, C., MAGNAUDET, J. & TCHOUFAG, J. 2016 Paths and wakes of deformable nearly spheroidal rising bubbles close to the transition to path instability. *Phys. Rev. Fluids* **1** (5), 053604.

CARTER, D.W. & COLETTI, F. 2017 Scale-to-scale anisotropy in homogeneous turbulence. *J. Fluid Mech.* **827**, 250–284.

CHENG, K.K. & PARK, C. 2017 Surface tension of dilute alcohol–aqueous binary fluids: n-butanol/water, n-pentanol/water, and n-hexanol/water solutions. *Heat Mass Transfer* **53**, 2255–2263.

DU CLUZEAU, A., BOIS, G., LEONI, N. & TOUTANT, A. 2022 Analysis and modeling of bubble-induced agitation from direct numerical simulation of homogeneous bubbly flows. *Phys. Rev. Fluids* **7** (4), 044604.

DU CLUZEAU, A., BOIS, G. & TOUTANT, A. 2019 Analysis and modelling of Reynolds stresses in turbulent bubbly up-flows from direct numerical simulations. *J. Fluid Mech.* **866**, 132–168.

CRAIG, V.S.J., NINHAM, B.W. & PASHLEY, R.M. 1993 Effect of electrolytes on bubble coalescence. *Nature* **364** (6435), 317–319.

CUENOT, B., MAGNAUDET, J. & SPENNATO, B. 1997 The effects of slightly soluble surfactants on the flow around a spherical bubble. *J. Fluid Mech.* **339**, 25–53.

DRENCKHAN, W. & SAINT-JALMES, A. 2015 The science of foaming. *Adv. Colloid Interface Sci.* **222**, 228–259.

DURST, F., SCHÖNUNG, B., SELANGER, K. & WINTER, M. 1986 Bubble-driven liquid flows. *J. Fluid Mech.* **170**, 53–82.

EFTEKHARI, M., SCHWARZENBERGER, K., HEITKAM, S., JAVADI, A., BASHKATOV, A., ATA, S. & ECKERT, K. 2021 Interfacial behavior of particle-laden bubbles under asymmetric shear flow. *Langmuir* **37** (45), 13244–13254.

ELLINGSEN, K. & RISSO, F. 2001 On the rise of an ellipsoidal bubble in water: oscillatory paths and liquid-induced velocity. *J. Fluid Mech.* **440**, 235–268.

FRISCH, U. 1995 *Turbulence: The Legacy of A.N. Kolmogorov*. Cambridge University Press.

FRUMKIN, A. & LEVICH, V.G. 1947 On surfactants and interfacial motion. *Zh. Fiz. Khim.* **21**, 1183–1204.

GVOZDIĆ, B., DUNG, O.-Y., VAN GILS, D.P.M., BRUGGERT, G.-W.H., ALMÉRAS, E., SUN, C., LOHSE, D. & HUISMAN, S.G. 2019 Twente mass and heat transfer water tunnel: temperature controlled turbulent multiphase channel flow with heat and mass transfer. *Rev. Sci. Instrum.* **90** (7), 075117.

HAYASHI, K. & TOMIYAMA, A. 2018 Effects of surfactant on lift coefficients of bubbles in linear shear flows. *Intl J. Multiphase Flow* **99**, 86–93.

HESSENKEMPER, H., STARKE, S., ATASSI, Y., ZIEGENHEIN, T. & LUCAS, D. 2022 Bubble identification from images with machine learning methods. *Intl J. Multiphase Flow* **155**, 104169.

HESSENKEMPER, H. & ZIEGENHEIN, T. 2018 Particle shadow velocimetry (PSV) in bubbly flows. *Intl J. Multiphase Flow* **106**, 268–279.

HESSENKEMPER, H., ZIEGENHEIN, T., LUCAS, D. & TOMIYAMA, A. 2021*a* Influence of surfactant contaminations on the lift force of ellipsoidal bubbles in water. *Intl J. Multiphase Flow* **145**, 103833.

HESSENKEMPER, H., ZIEGENHEIN, T., RZEHAK, R., LUCAS, D. & TOMIYAMA, A. 2021*b* Lift force coefficient of ellipsoidal single bubbles in water. *Intl J. Multiphase Flow* **138**, 103587.

HORI, Y., BOTHE, D., HAYASHI, K., HOSOKAWA, S. & TOMIYAMA, A. 2020 Mass transfer from single carbon-dioxide bubbles in surfactant–electrolyte mixed aqueous solutions in vertical pipes. *Intl J. Multiphase Flow* **124**, 103207.

HOROWITZ, M. & WILLIAMSON, C.H.K. 2010 The effect of Reynolds number on the dynamics and wakes of freely rising and falling spheres. *J. Fluid Mech.* **651**, 251–294.

INNOCENTI, A., JACCOD, A., POPINET, S. & CHIBBARO, S. 2021 Direct numerical simulation of bubble-induced turbulence. *J. Fluid Mech.* **918**, A23.

LAI, C.C.K. & SOCOLOFSKY, S.A. 2019 The turbulent kinetic energy budget in a bubble plume. *J. Fluid Mech.* **865**, 993–1041.

LANCE, M. & BATAILLE, J. 1991 Turbulence in the liquid phase of a uniform bubbly air–water flow. *J. Fluid Mech.* **222**, 95–118.

LANGEVIN, D. 2014 Rheology of adsorbed surfactant monolayers at fluid surfaces. *Annu. Rev. Fluid Mech.* **46**, 47–65.

LEGENDRE, D., LAUGA, E. & MAGNAUDET, J. 2009 Influence of slip on the dynamics of two-dimensional wakes. *J. Fluid Mech.* **633**, 437–447.

LEVICH, V.G. 1962 *Physicochemical Hydrodynamics*. Prentice-Hall.

LIAO, Y. & MA, T. 2022 Study on bubble-induced turbulence in pipes and containers with Reynolds-stress models. *Exp. Comput. Multiphase Flow* **4** (2), 121–132.

LOHSE, D. 2018 Bubble puzzles: from fundamentals to applications. *Phys. Rev. Fluids* **3** (11), 110504.

LOHSE, D. 2022 Fundamental fluid dynamics challenges in inkjet printing. *Annu. Rev. Fluid Mech.* **54**, 349–382.

LOUBIÈRE, K. & HÉBRARD, G. 2004 Influence of liquid surface tension (surfactants) on bubble formation at rigid and flexible orifices. *Chem. Engng Process* **43** (11), 1361–1369.

LU, J., MURADOGLU, M. & TRYGGVASON, G. 2017 Effect of insoluble surfactant on turbulent bubbly flows in vertical channels. *Intl J. Multiphase Flow* **95**, 135–143.

LU, J. & TRYGGVASON, G. 2013 Dynamics of nearly spherical bubbles in a turbulent channel upflow. *J. Fluid Mech.* **732**, 166–189.

MA, T., HESSENKEMPER, H., LUCAS, D. & BRAGG, A.D. 2022 An experimental study on the multiscale properties of turbulence in bubble-laden flows. *J. Fluid Mech.* **936**, A42.

MA, T., HESSENKEMPER, H., LUCAS, D. & BRAGG, A.D. 2023 Fate of bubble clusters rising in a quiescent liquid. *J. Fluid Mech.* (under revision), arXiv:2306.02101.

MA, T., LUCAS, D. & BRAGG, A.D. 2020*a* Explicit algebraic relation for calculating Reynolds normal stresses in flows dominated by bubble-induced turbulence. *Phys. Rev. Fluids* **5**, 084305.

MA, T., LUCAS, D., JAKIRLIĆ, S. & FRÖHLICH, J. 2020*b* Progress in the second-moment closure for bubbly flow based on direct numerical simulation data. *J. Fluid Mech.* **883**, A9.

MA, T., OTT, B., FRÖHLICH, J. & BRAGG, A.D. 2021 Scale-dependent anisotropy, energy transfer and intermittency in bubble-laden turbulent flows. *J. Fluid Mech.* **927**, A16.

MA, T., SANTARELLI, C., ZIEGENHEIN, T., LUCAS, D. & FRÖHLICH, J. 2017 Direct numerical simulation-based Reynolds-averaged closure for bubble-induced turbulence. *Phys. Rev. Fluids* **2**, 034301.

MAEDA, K., DATE, M., SUGIYAMA, K., TAKAGI, S. & MATSUMOTO, Y. 2021 Viscid-inviscid interactions of pairwise bubbles in a turbulent channel flow and their implications for bubble clustering. *J. Fluid Mech.* **919**, A30.

MAGNAUDET, J. & EAMES, I. 2000 The motion of high-Reynolds-number bubbles in inhomogeneous flows. *Annu. Rev. Fluid Mech.* **32** (1), 659–708.

MANIKANTAN, H. & SQUIRES, T.M. 2020 Surfactant dynamics: hidden variables controlling fluid flows. *J. Fluid Mech.* **892**, P1.

MASUK, A.U.M., SALIBINDLA, A.K.R. & NI, R. 2021 Simultaneous measurements of deforming Hinze-scale bubbles with surrounding turbulence. *J. Fluid Mech.* **910**, A21.

MATHAI, V., LOHSE, D. & SUN, C. 2020 Bubbly and buoyant particle-laden turbulent flows. *Annu. Rev. Condens. Matter Phys.* **11**, 529–559.

MATHAI, V., ZHU, X., SUN, C. & LOHSE, D. 2018 Flutter to tumble transition of buoyant spheres triggered by rotational inertia changes. *Nat. Commun.* **9** (1), 1792.

MCLAUGHLIN, J.B. 1996 Numerical simulation of bubble motion in water. *J. Colloid Interface Sci.* **184** (2), 614–625.

MENDEZ-DIAZ, S., SERRANO-GARCÍA, J.C., ZENIT, R. & HERNÁNDEZ-CORDERO, J.A. 2013 Power spectral distributions of pseudo-turbulent bubbly flows. *Phys. Fluids* **25**, 043303.

MOORE, D.W. 1963 The boundary layer on a spherical gas bubble. *J. Fluid Mech.* **16** (2), 161–176.

MOUGIN, G. & MAGNAUDET, J. 2002 Path instability of a rising bubble. *Phys. Rev. Lett.* **88** (1), 014502.

MOUGIN, G. & MAGNAUDET, J. 2006 Wake-induced forces and torques on a zigzagging/spiralling bubble. *J. Fluid Mech.* **567**, 185–194.

NÉEL, B. & DEIKE, L. 2021 Collective bursting of free-surface bubbles, and the role of surface contamination. *J. Fluid Mech.* **917**, A46.

PALAPARTHI, R., PAPAGEORGIOU, D.T. & MALDARELLI, C. 2006 Theory and experiments on the stagnant cap regime in the motion of spherical surfactant-laden bubbles. *J. Fluid Mech.* **559**, 1–44.

PANDEY, V., RAMADUGU, R. & PERLEKAR, P. 2020 Liquid velocity fluctuations and energy spectra in three-dimensional buoyancy-driven bubbly flows. *J. Fluid Mech.* **884**, R6.

PESCI, C., WEINER, A., MARSCHALL, H. & BOTHE, D. 2018 Computational analysis of single rising bubbles influenced by soluble surfactant. *J. Fluid Mech.* **856**, 709–763.

POPE, S.B. 2000 *Turbulent Flows*, 1st edn. Cambridge University Press.

QI, Y., TAN, S., CORBITT, N., URBANIK, C., SALIBINDLA, A.K.R. & NI, R. 2022 Fragmentation in turbulence by small eddies. *Nat. Commun.* **13** (1), 469.

RENSEN, J., LUTHER, S. & LOHSE, D. 2005 The effect of bubbles on developed turbulence. *J. Fluid Mech.* **538**, 153–187.

RIBOUX, G., LEGENDRE, D. & RISSO, F. 2013 A model of bubble-induced turbulence based on large-scale wake interactions. *J. Fluid Mech.* **719**, 362–387.

RIBOUX, G., RISSO, F. & LEGENDRE, D. 2010 Experimental characterization of the agitation generated by bubbles rising at high Reynolds number. *J. Fluid Mech.* **643**, 509–539.

RISSO, F. 2018 Agitation, mixing, and transfers induced by bubbles. *Annu. Rev. Fluid Mech.* **50**, 25–48.

ROGHAIR, I., MERCADO, J.M., VAN SINT ANNALAND, M., KUIPERS, H., SUN, C. & LOHSE, D. 2011 Energy spectra and bubble velocity distributions in pseudo-turbulence: numerical simulations vs experiments. *Intl J. Multiphase Flow* **37**, 1093–1098.

SALIBINDLA, A.K.R., MASUK, A.U.M., TAN, S. & NI, R. 2020 Lift and drag coefficients of deformable bubbles in intense turbulence determined from bubble rise velocity. *J. Fluid Mech.* **894**, A20.

SANTARELLI, C., ROUSSEL, J. & FRÖHLICH, J. 2016 Budget analysis of the turbulent kinetic energy for bubbly flow in a vertical channel. *Chem. Engng Sci.* **141**, 46–62.

SCHLÜTER, M., HERRES-PAWLIS, S., NIEKEN, U., TUTTLIES, U. & BOTHE, D. 2021 Small-scale phenomena in reactive bubbly flows: experiments, numerical modeling, and applications. *Annu. Rev. Chem. Biomol. Engng* **12**, 625–643.

SHEW, W.L. & PINTON, J.-F. 2006 Dynamical model of bubble path instability. *Phys. Rev. Lett.* **97** (14), 144508.

SOLIGO, G., ROCCON, A. & SOLDATI, A. 2019 Breakage, coalescence and size distribution of surfactant-laden droplets in turbulent flow. *J. Fluid Mech.* **881**, 244–282.

SREENIVASAN, K.R. & ANTONIA, R.A. 1997 The phenomenology of small-scale turbulence. *Annu. Rev. Fluid Mech.* **29** (1), 435–472.

STONE, H.A. 1994 Dynamics of drop deformation and breakup in viscous fluids. *Annu. Rev. Fluid Mech.* **26** (1), 65–102.

TAGAWA, Y., TAKAGI, S. & MATSUMOTO, Y. 2014 Surfactant effect on path instability of a rising bubble. *J. Fluid Mech.* **738**, 124.

TAKAGI, S. & MATSUMOTO, Y. 2011 Surfactant effects on bubble motion and bubbly flows. *Annu. Rev. Fluid Mech.* **43**, 615–636.

TAKAGI, S., OGASAWARA, T., FUKUTA, M. & MATSUMOTO, Y. 2009 Surfactant effect on the bubble motions and bubbly flow structures in a vertical channel. *Fluid Dyn. Res.* **41** (6), 065003.

TAKAGI, S., OGASAWARA, T. & MATSUMOTO, Y. 2008 The effects of surfactant on the multiscale structure of bubbly flows. *Phil. Trans. R. Soc.* A **366** (1873), 2117–2129.

TOMIYAMA, A., CELATA, G.P., HOSOKAWA, S. & YOSHIDA, S. 2002 Terminal velocity of single bubbles in surface tension force dominant regime. *Intl J. Multiphase Flow* **28** (9), 1497–1519.

TOWNSEND, A. 1949 The fully developed wake of a circular cylinder. *Austral. J. Chem.* **2** (4), 451–468.

VELDHUIS, C., BIESHEUVEL, A. & LOHSE, D. 2009 Freely rising light solid spheres. *Intl J. Multiphase Flow* **35** (4), 312–322.

VELDHUIS, C., BIESHEUVEL, A. & VAN WIJNGAARDEN, L. 2008 Shape oscillations on bubbles rising in clean and in tap water. *Phys. Fluids* **20** (4), 040705.

VERSCHOOF, R.A., VAN DER VEEN, R.C.A., SUN, C. & LOHSE, D. 2016 Bubble drag reduction requires large bubbles. *Phys. Rev. Lett.* **117** (10), 104502.

YBERT, C. & DI MEGLIO, J.-M. 1998 Ascending air bubbles in protein solutions. *Eur. Phys. J.* B **4** (3), 313–319.

YBERT, C. & DI MEGLIO, J.-M. 2000 Ascending air bubbles in solutions of surface-active molecules: influence of desorption kinetics. *Eur. Phys. J.* E **3** (2), 143–148.

ZIEGENHEIN, T. & LUCAS, D. 2017 Observations on bubble shapes in bubble columns under different flow conditions. *Expl Therm. Fluid Sci.* **85**, 248–256.

ZIEGENHEIN, T. & LUCAS, D. 2019 The critical bubble diameter of the lift force in technical and environmental, buoyancy-driven bubbly flows. *Intl J. Multiphase Flow* **116**, 26–38.